

NONLINEAR PULSATIONS OF RED SUPERGIANTS

Yu. A. Fadeyev¹

*Institute of Astronomy, Russian Academy of Sciences, Pyatnitskaya ul. 48, Moscow, 109017
Russia*

Received

Abstract — Excitation of radial oscillations in population I ($X = 0.7$, $Z = 0.02$) red supergiants is investigated using the solution of the equations of radiation hydrodynamics and turbulent convection. The core helium burning stars with masses $8M_{\odot} \leq M \leq 20M_{\odot}$ and effective temperatures $T_{\text{eff}} < 4000\text{K}$ are shown to be unstable against radial pulsations in the fundamental mode. The oscillation periods range between 45 and 1180 days. The pulsational instability is due to the κ -mechanism in the hydrogen and helium ionization zones. Radial pulsations of stars with mass $M < 15M_{\odot}$ are strictly periodic with the light amplitude $\Delta M_{\text{bol}} \leq 0^{\text{m}}.5$. The pulsation amplitude increases with increasing stellar mass and for $M > 15M_{\odot}$ the maximum expansion velocity of outer layers is as high as one third of the escape velocity. The mean radii of outer Lagrangean mass zones increase due to nonlinear oscillations by $\leq 30\%$ in comparison with the initial equilibrium. The approximate method (with uncertainty of a factor of 1.5) to evaluate the mass of the pulsating red supergiant with the known period of radial oscillations is proposed. The approximation of the pulsation constant Q as a function of the mass-to-radius ratio is given. Masses of seven galactic red supergiants are evaluated using the period-mean density relation.

Keywords: *stars: variable and peculiar.*

¹E-mail: fadeyev@inasan.ru

1 INTRODUCTION

Red supergiants are long-period variables with semiregular light variations on a timescale $\gtrsim 10^2$ day. The period–luminosity relation (Glass 1979; Feast et al. 1980) and the linear theory of adiabatic oscillations (Stothers 1969, 1972) allow us to suppose that such a type of variability is due to radial stellar pulsations. At the same time together with semiregular variability some red supergiants exhibit superimposed irregular light variations (Kiss et al. 2006). The secondary stochastic variability is thought to be due to the large-scale convection in the outer subphotospheric layers (Stothers and Leung 1971; Schwarzschild 1975; Stothers 2010). Red supergiants are also remarkable due to intensive mass loss revealed through a large infrared excess indicating dust production in the stellar wind (Verhoelst et al. 2009).

The period–luminosity relation of radially pulsating red supergiants is used for determination of extra-galactic distances and in comparison with Cepheids the red supergiants allow us to substantially extend the distance scale due to their higher luminosities (Pierce et al. 2000; Jurcevic et al. 2000). Application of the theory of stellar pulsation to the analysis of observed variability of red supergiants allows us to verify some conclusions of the stellar evolution theory in a way similar to that employed earlier for Cepheids. It should be noted also that the growing bulk of recent observations indicate that the strong stellar wind of massive late-type supergiants is due to nonlinear stellar oscillations (van Loon et al. 2008)

The nature of radial oscillations in red supergiants is still not completely clear yet. The linear analysis of pulsational instability of red supergiants with masses $15M_{\odot} \leq M \leq 30M_{\odot}$ was performed by Li and Gong (1994) and Guo and Li (2002). According to their calculations radial oscillations of red supergiants are due to instability of the fundamental mode and, perhaps, the first overtone. However the theoretical period–luminosity relation agrees only with fundamental mode oscillations.

Nonlinear radial oscillations of red supergiants were considered only in two studies. In the first one (Heger et al. 1997) the authors investigated radial oscillations of the red supergiant with mass $M = 15M_{\odot}$ at the final stage of the core helium burning. In the second work (Yoon and Cantiello 2010) the authors investigated pulsational instability of red supergiants with masses $15M_{\odot} \leq M \leq 40M_{\odot}$. It should be noted that in both these studies the self-exciting stellar oscillations were treated with modified methods of stellar evolution calculation and effects of interaction between pulsation motions and turbulent convection were not taken into account.

Below we present results of investigation of nonlinear pulsations of red supergiants obtained from the self-consistent solution of the equations of radiation hydrodynamics and turbulent convection. The need for such an approach is due to the significant length and mass of the

outer convection zone involved in pulsation motions. The treatment of convective heat transport uses the solution of the diffusion-type equations for the enthalpy and the mean turbulent energy obtained by Kuhfuß(1986) for spherically-symmetric gas flows from the Navier-Stokes equation. Thus, the results presented below deal with modelling the semiregular variability and the secondary stochastic variability is not considered because this problem is beyond the approximation of spherical geometry. We consider the stars with masses at the zero-age main sequence $8M_{\odot} \leq M_{\text{ZAMS}} \leq 20M_{\odot}$ and initial fractional mass abundances of hydrogen and elements heavier than helium $X = 0.7$ and $Z = 0.02$.

2 INITIAL CONDITIONS

The problem of self-exciting stellar oscillations is the Cauchy problem for equations of hydrodynamics with initial conditions corresponding to the hydrostatic and thermal equilibrium. In the present study the initial conditions were taken from the evolutionary models of stars at the core helium burning. Methods of stellar evolution calculations are discussed in our previous papers (Fadeyev 2011a, b).

The evolutionary tracks in the Hertzsprung-Russel (HR) diagram of population I stars ($X = 0.7$, $Z = 0.02$) with initial masses $M_{\text{ZAMS}} = 10, 15$ and $20M_{\odot}$ are shown in Fig. 1. Final points of tracks correspond to helium exhaustion in the stellar core ($Y_c \approx 10^{-4}$). Solid lines indicate parts of tracks when the star is the core helium burning red supergiant with effective temperature $T_{\text{eff}} \leq 4000$ K.

The star leaves the main sequence after core hydrogen exhaustion and crosses the HR diagram to lower effective temperatures where becomes the red supergiant with gradually increasing luminosity. However, from the observational point of view the red supergiants with gravitationally contracting helium core are not interesting since this evolutionary stage proceeds in the Kelvin-Helmholtz time scale. For example, for the star with initial mass $M_{\text{ZAMS}} = 10M_{\odot}$ the duration of gravitational contraction of the helium core is $\approx 10^5$ years.

The luminosity ceases to increase when the triple alpha process becomes the main energy source in the stellar center. For the star with initial mass $M_{\text{ZAMS}} = 10M_{\odot}$ the total duration of thermonuclear helium burning is $\approx 2.8 \cdot 10^6$ years and in the beginning the star remains the red supergiant with luminosity decreasing by a factor of two during $\approx 1.2 \cdot 10^6$ years. The star leaves the red supergiant domain when the central helium abundance decreases below $Y_c \approx 0.52$ and its evolutionary track loops the HR diagram to effective temperatures as high as $T_{\text{eff}} \approx 10^4$ K. The star becomes again the red supergiant when its central helium abundance decreases to $Y_c \approx 0.05$ and the time of helium exhaustion does not exceed $2 \cdot 10^5$ years. Therefore, of most interest is the initial stage of helium burning during of which the luminosity of the red

supergiant decreases. Evolution of stars with initial masses $M_{\text{ZAMS}} < 15M_{\odot}$ is nearly the same but proceeds in different time scales.

Evolutionary tracks of the core helium burning stars $M_{\text{ZAMS}} \geq 15M_{\odot}$ do not loop in the HR diagram and all the time remain in the red supergiant domain. For $M_{\text{ZAMS}} = 20M_{\odot}$ the core helium burning proceeds during $\approx 8.4 \cdot 10^5$ years, in the beginning during $\approx 3.6 \cdot 10^5$ years the stellar luminosity decreasing and then increasing to $L \approx 10^5 L_{\odot}$.

All red supergiant evolutionary models used as initial conditions for hydrodynamic computations are chemically homogeneous between the inner boundary to the stellar surface. Moreover, for the given value of M_{ZAMS} the abundances in the stellar envelope do not change during the core helium burning. This is due to the fact that the size of the outer convective zone is maximum at the final stage of gravitational contraction of the helium core just before ignition of the triple alpha process. Depending on the mass and luminosity of the star the radius of the inner boundary r_0 ranges within $0.01 \lesssim r_0/R_{\text{eq}} < 0.1$, where R_{eq} is the radius of the upper boundary of the equilibrium model.

3 RESULTS OF HYDRODYNAMIC COMPUTATIONS

The method for the self-consistent solution of the equations of radiation hydrodynamics and turbulent convection is described in our previous paper (Fadeyev, 2011b), so that below we only discuss the results obtained. Computations were carried out with the number of Lagrangean mass zones $500 \leq N \leq 10^3$. To be confident that the solution is independent of the inner boundary radius r_0 and the number of Lagrangean zones N some hydrodynamic models were computed with several different values of these quantities.

Our hydrodynamic computations show that red supergiants with initial masses $8M_{\odot} \leq M_{\text{ZAMS}} \leq 20M_{\odot}$ are unstable against radial oscillations in the fundamental mode. However depending on the value of M_{ZAMS} hydrodynamic models demonstrate different behaviour both during the growth of instability and after the limit amplitude attainment. In particular, in stars with initial mass $M_{\text{ZAMS}} < 15M_{\odot}$ the oscillation amplitude is always enough small, whereas for $M_{\text{ZAMS}} > 15M_{\odot}$ nonlinear effects play a substantial role.

The main properties of hydrodynamical models are summarized in Table 1, where the bolometric luminosity L and the effective temperature T_{eff} correspond to the initial equilibrium model, Y_c is the fractional helium abundance in the stellar center, Π and Q are the pulsation period and the pulsation constant in days, $\eta = \Pi d \ln E_K / dt$ is the growth rate of the pulsation kinetic energy E_K . Reciprocal of this quantity equals the number of pulsation periods during which the kinetic energy increases by a factor of $e = 2.718 \dots$. Ratios of the outer boundary mean radius $\langle R \rangle$ to the equilibrium radius of the model R_{eq} are given in the last column of

Table 1 and show the role of nonlinear effects after the limit amplitude attainment.

The oscillation amplitude of red supergiants $M_{\text{ZAMS}} = 10M_{\odot}$ at the top of the evolutionary track is enough small and the relative radial displacement of the upper boundary is $\Delta R/R_{\text{eq}} = 0.06$. The oscillation amplitude gradually increases with decreasing luminosity and in the point with minimum luminosity before the loop in the HR diagram $\Delta R/R_{\text{eq}} = 0.13$. Enhancement of the radial oscillation amplitude with decreasing luminosity is illustrated in Fig. 2 where variations of the velocity at the upper boundary U and the bolometric magnitude M_{bol} are shown for $L = 2 \cdot 10^4$, $1.5 \cdot 10^4$ and $10^4 L_{\odot}$.

Fairly good repetition of small amplitude oscillations allows us to calculate the mechanical work done by Lagrangean mass zones and thereby to evaluate their contribution into excitation or damping of instability. The radial dependence of the mechanical work $\oint P dV$, where V is the specific volume and P is the sum of gas, radiation and turbulent pressure, is shown in Fig. 3 for the hydrodynamical model $M_{\text{ZAMS}} = 10M_{\odot}$, $L = 1.5 \cdot 10^5 L_{\odot}$. The region of instability excitation ($\oint P dV > 0$) encompasses the layers with temperature $1.2 \cdot 10^4 \lesssim T \lesssim 4 \cdot 10^4 \text{K}$ corresponding to the hydrogen and helium ionization zones. In deeper layers ($T > 4 \cdot 10^4 \text{K}$) with fully ionized helium the pulsational instability is damped ($\oint P dV < 0$).

To understand the physical mechanism of excitation of pulsational instability let us consider variations of the gas density ρ , temperature T , opacity κ and luminosity $L_{\text{rad}} = 4\pi r^2 F_{\text{rad}}$, where F_{rad} is radiative flux, in Lagrangean mass zones of the hydrodynamical model. In Fig. 4(a) we give the plots of relative variations $\delta\rho/\rho$, $\delta T/T$ and $\delta\kappa/\kappa$ in the layers of fully ionized helium with temperature ranging within $4.9 \cdot 10^4 \text{K} \leq T \leq 5.6 \cdot 10^4 \text{K}$. For the sake of convenience, the plots are arbitrarily shifted along the vertical axis. Coincidence of the maxima of density and temperature variations indicates that oscillations are nearly adiabatic. Decrease of opacity at maximum compression damps the instability because, as seen in Fig. 4(b), heat losses due to radiation reach their maximum.

Variations of same quantities for the layer with temperature $1.4 \cdot 10^4 \text{K} \leq T \leq 1.7 \cdot 10^4 \text{K}$ corresponding to partial helium ionization are plotted in Fig. 5. Substantial phase shifts between maxima of density and temperature indicate large nonadiabaticity of pulsation motions, whereas the delay of the maximum temperature with respect to maximum compression is the cause of the positive mechanical work. Absorption of heat during compression is due to increase of opacity and it is accompanied by decrease of the radiative flux.

Thus, damping of oscillations in the layers of fully ionized helium and driving of pulsational instability in the hydrogen and helium ionization zones are due to the κ -mechanism, because effects of heat gains and losses are connected with absorption and emission of radiation. Low rates of the instability growth ($\eta \sim 10^{-2}$) and the small limit cycle amplitude are due to the

small fraction of radiation in the total energy flux ($L_{\text{rad}} \lesssim 10^{-2} L_r$). Driving of pulsational instability at so small radiation fluxes is due to the large amplitude of total luminosity variations. As seen in Fig. 6, the amplitude of luminosity variations is largest in vicinity of the helium ionization zone.

Pulsational instability of red supergiants increases with increasing initial stellar mass and for $M_{\text{ZAMS}} > 15M_{\odot}$ nonlinear effects become significant. In Fig. 7 we give the temporal dependences of the kinetic energy E_K of the pulsating envelope and the radius of the upper boundary R in units of the equilibrium radius R_{eq} for the red supergiant model with initial mass $M_{\text{ZAMS}} = 16M_{\odot}$ and luminosity $L = 8.5 \cdot 10^4 L_{\odot}$. Compared to less massive supergiants this model demonstrates the growth rate which is higher by an order of magnitude, whereas after the attainment of the limiting amplitude the mean radii of outer Lagrangean mass zones exceed their equilibrium values by nearly one third. The amplitude ceases to grow in a transitional process encompassing roughly a dozen of oscillation periods ($20 < t/\Pi < 30$). During this time interval the sources of instability in the hydrogen and helium ionization zones are balanced by damping of instability in layers of fully ionized helium and shock radiative losses in the layers above the photosphere.

4 PERIOD–LUMINOSITY RELATION

In the HR diagram red supergiants occupy the domain with relatively narrow effective temperature range ($3000 \text{ K} \lesssim T_{\text{eff}} \lesssim 4000 \text{ K}$), so that similar to Cepheids they exhibit correlation between the equilibrium luminosity L and the period of radial pulsations Π . From observations such a correlation is known as the period–luminosity relation. The theoretical period–luminosity relation obtained in the present study is shown in Fig. 8 for models of three evolutionary sequences with initial masses $M_{\text{ZAMS}} = 10, 15$ and $20M_{\odot}$. Hydrodynamical models of red giants at the evolutionary stage of decreasing luminosity are shown by filled circles and the dashed lines show the linear fits for each evolutionary sequence.

For stars with initial mass $M_{\text{ZAMS}} = 10M_{\odot}$ the evolutionary track loops the HR diagram during helium burning and three models shown in Fig. 8 by triangles correspond to the initial part of the loop with effective temperatures $T_{\text{eff}} < 4000 \text{ K}$. Therefore, one of the causes of the dispersion of points in the empirical period–luminosity diagram is that some stars with masses $M < 15M_{\odot}$ leave the red supergiant domain and others return to it.

The chemical composition of outer layers involved in pulsation motions does not change, whereas effects of mass loss for $M < 15M_{\odot}$ are insignificant. Therefore, red supergiants with almost exhausted helium in the stellar center obey the same period–luminosity relation as stars in earlier phases of helium burning. This is illustrated in Fig. 8 where two models of stars

$M_{\text{ZAMS}} = 10M_{\odot}$ with central helium abundances $Y_c = 2.4 \cdot 10^{-3}$ and $1.1 \cdot 10^{-4}$ are shown by open circles.

As can be seen in Fig. 8, the dispersion of the common correlation between the period and luminosity of red supergiants is due to dependence of the both luminosity and period on the stellar mass. Therefore, one of the causes of dispersion on the empirical period–luminosity diagram is due to different masses of observed stars. It should also be noted that the mass–luminosity relation of red supergiants and, therefore, the period–luminosity relation, depend on convective overshooting and mass loss during the preceding evolution. An important role in the both mass–luminosity and period–luminosity relations belongs also to abundances of heavy elements Z . These effects, however, were beyond the scope of the present study.

5 PERIOD–MASS DIAGRAM

The equilibrium luminosity of the red supergiant during helium burning changes within the ranges that depend on the initial stellar mass. For example, in stars with $M_{\text{ZAMS}} \approx 10M_{\odot}$ the luminosity decreases by a half, whereas in red supergiants with initial mass $M_{\text{ZAMS}} = 20M_{\odot}$ the maximum to minimum luminosity ratio decreases to ≈ 1.6 . The period of radial pulsations Π changes simultaneously with equilibrium luminosity L . Evolution of red supergiants $M_{\text{ZAMS}} \leq 12M_{\odot}$ between the upper and lower luminosity limits is accompanied by the change of the pulsation period by a factor of three. The maximum to minimum period ratio decreases to a factor of two for $M_{\text{ZAMS}} = 20M_{\odot}$.

This property of red supergiants is illustrated in Fig. 9 where for stars with initial masses $8M_{\odot} \leq M_{\text{ZAMS}} \leq 20M_{\odot}$ we show the period–mass diagram. Hydrodynamical models of stars at the top of the evolutionary track are shown by filled circles. Open circles indicate the red supergiant models with lower luminosity. The diagram in Fig. 9 takes into account effects of mass loss and along the vertical axis we give the mass values M of evolving stars. Evolution of the red supergiant corresponds to the displacement on the diagram from right to left and then in the opposite direction. For models $M_{\text{ZAMS}} = 10M_{\odot}$ and $20M_{\odot}$ this displacement is shown by arrows.

The period–mass diagram in Fig. 9 demonstrates the existence of the limited area of mass and period values. The borders of allowed masses and periods of radially pulsating red supergiants can be approximately fitted as

$$\log(M/M_{\odot}) = \begin{cases} 0.153 + 0.365 \log \Pi \\ 0.488 + 0.273 \log \Pi \end{cases} \quad (1)$$

and in Fig. 9 they are shown by dashed lines. Thus, from the observational estimate of the

period Π relations (1) allow us to evaluate the upper and lower mass limits of the red supergiant. For periods $\Pi \leq 300$ the uncertainty of such an estimate is about a factor of ≈ 1.5 .

6 PULSATION CONSTANT

The more exact value of the red supergiant mass can be obtained from the period–mean density relation

$$\Pi = Q (R/R_{\odot})^{3/2} (M/M_{\odot})^{-1/2} \quad (2)$$

provided that the pulsation period Π and the mean stellar radius R are known from observations. The pulsation constant Q is obtained from the theory of stellar pulsation and in some cases can be expressed as a function of the stellar mass M and stellar radius R . Substitution of this expression into the period–mean density relation (2) allows us to obtain the explicit expression for the mass of the pulsating star.

The pulsation constants obtained in our hydrodynamical calculations of red supergiants with initial masses $8M_{\odot} \leq M_{\text{ZAMS}} \leq 20M_{\odot}$ and pulsation periods $45 \leq \Pi \leq 1180$ are shown in Fig. 10 as a function of mass–to–radius ratio $f = (M/M_{\odot})/(R/R_{\odot})$. The linear fit of the pulsation constant is written as

$$\log Q = -2.288 - 0.778 \log f \quad (3)$$

and is shown in Fig. 10 by the dashed line.

Masses M of seven galactic red supergiants evaluated from substitution of (3) into the period–mean density relation (2) are given in Table 2. The periods Π are taken from the General Catalogue of Variable Stars (Samus et al. 2011). The mean stellar radii were evaluated by Levesque et al. (2005) and Josselin and Plez (2007). In last two columns of Table 2 we give the lower M_a and upper M_b mass limits derived from (1).

Unfortunately, the existing estimates of mean radii of red supergiants are still highly uncertain. For example, the uncertainty in the effective temperature is $\approx 25\%$ (Josselin and Plez 2007), so that the uncertainty in the mean radius is as high as $\approx 60\%$. Therefore, the case when the stellar mass determined from the period–mean density relation is beyond the interval $[M_a, M_b]$ should not be considered as a contradiction. For example, if we adopt that the radius of AD Per is larger by 20% ($R = 548R_{\odot}$) then the stellar mass is $M = 12.3M_{\odot}$, that is within ranges given by (1).

7 CONCLUSION

Given in the previous section estimates of masses of seven galactic red supergiants allow us to conclude that the theory of stellar evolution is in an agreement with observational estimates of stellar radii. To compare more stars with the theoretical period–luminosity relation one should consider pulsational instability of red supergiants in the wider interval of initial masses M_{ZAMS} .

For more detailed theoretical period–luminosity relation one should consider the role of some parameters used in evolutionary computations. One of them is the overshooting parameter. In the present study the evolutionary computations were done for the ratio of the overshooting distance to the pressure scale height $l_{\text{ov}}/H_{\text{P}} = 0.15$. The need to know the role of this parameter is due to the dependence of the mass–luminosity relation of helium burning stars on convective overshooting.

In stars with masses $M \geq 20M_{\odot}$ effects of mass loss during the red supergiant evolutionary stage become significant. In the present study the evolutionary calculations were done with mass loss rates by Nieuwenhuijzen and de Jager (1990) however determination of the mass loss rate \dot{M} as a function of fundamental stellar parameters remains disputable (Mauron and Josselin, 2011) Therefore, one should employ parametrization of the expression for \dot{M} and consider the mass–luminosity and period–luminosity relations as a function of this parameter.

Another parameter which significantly affects the period–luminosity relation of red supergiants is the mass fraction abundance of heavy elements Z . Of special interest is the period–luminosity relation for $Z = 0.008$ which is typical for the Large and Small Magellanic Clouds.

REFERENCES

1. Yu.A. Fadeyev, Pis'ma Astron. Zh. **37**, 13 (2011a) [Astron.Lett. **37**, 11 (2011a)].
2. Yu.A. Fadeyev, Pis'ma Astron. Zh. **37**, 440 (2011a) [Astron.Lett. **37**, 403 (2011b)].
3. M.W. Feast, R.M. Catchpole, D.S. Carter, et al., MNRAS **193**, 377 (1980).
4. I.S. Glass, MNRAS **186**, 317 (1979).
5. J.H. Guo and Y. Li, Astrophys.J **565**, 559 (2002).
6. A. Heger, L. Jeannin, N. Langer, et al., Astron.Astrophys. **327**, 224 (1997).
7. E. Josselin and B. Plez, Astron.Astrophys. **469**, 671 (2007).
8. J.S. Jurcevic, M.J. Pierce, and G.H. Jacoby, MNRAS **313**, 868 (2000).
9. L.L. Kiss, Gy.M. Szabó, and T.R. Bedding, MNRAS **372**, 1721 (2006).
10. R. Kuhfuß, 1986, Astron.Astrophys. **160**, 116 (1986).
11. E. Levesque, P. Massey, K.A.G. Olsen, et al., Astrophys.J. **628**, 973 (2005).
12. Y. Li and Z.G. Gong, Astron.Astrophys. **289**, 449 (1994).
13. J.Th. van Loon, M. Cohen, J.M. Oliveira, et al., Astron.Astrophys. **487**, 1055 (2008).
14. N. Maunon and E. Josselin, Astron.Astrophys. **526**, in press (2011).
15. H. Nieuwenhuijzen and C. de Jager, Astron.Astrophys. **231**, 134 (1990).
16. M.J. Pierce, J.S. Jurcevic, and D. Crabtree, MNRAS **313**, 271 (2000).
17. N.N. Samus, E.V. Kazarovets, N.N. Kireeva, et al. General Catalogue of Variable Stars (2011).
18. M. Schwarzschild, Astrophys.J. **195**, 137 (1975).
19. R. Stothers, Astrophys.J **156**, 541 (1969).
20. R. Stothers, Astron.Astrophys. **18**, 325 (1972).
21. R. Stothers, Astrophys.J **725**, 1170 (2010).
22. R. Stothers, K.C. Leung, Astron.Astrophys. **10**, 290 (1971).

- 23. T. Verhoelst, N. Van der Zypen, S. Hony, et al., *Astron.Astrophys.* **498**, 127 (2009).
- 24. S.-C. Yoon and M. Cantiello, *Astrophys.J.* **717**, L62 (2010).

Table 1: Hydrodynamical models of red supergiants.

$M_{\text{ZAMS}}/M_{\odot}$	M/M_{\odot}	$L/L_{\odot},$ 10^4	$T_{\text{eff}},$ K	Y_{c}	$\Pi,$ day	$Q,$ day	η	$\langle R \rangle / R_{\text{eq}}$
20	19.53	14.029	3320	0.975	1178	0.1365		
	18.36	9.380	3478	0.746	608	0.1058	0.27	1.24
	17.47	8.782	3522	0.480	555	0.1028	0.30	1.11
15	14.80	7.176	3370	0.968	651	0.1131	0.18	1.26
	14.12	4.454	3556	0.680	310	0.0883	0.10	1.12
	13.69	4.074	3620	0.379	262	0.0830	0.11	1.11
10	9.88	2.055	3570	0.970	203	0.0867	0.01	1.15
	9.76	1.507	3672	0.816	127	0.0747	0.03	1.10
	9.66	1.102	3870	0.523	67	0.0615	0.03	1.04
9	8.90	1.452	3610	0.973	154	0.0849	0.02	1.16
	8.76	0.668	3958	0.580	45	0.0574	0.02	1.02
8	7.02	0.962	3690	0.972	102	0.0765	0.02	1.13

Table 2: Masses of galactic red supergiants.

	Π , day	R/R_{\odot}	M/M_{\odot}	M_a/M_{\odot}	M_b/M_{\odot}
SU Per	533	780	17.1	14.1	17.1
W Per	485	620	12.2	13.6	16.6
V602 Car	635	860	17.7	15.0	17.9
AD Per	362.5	457	8.9	12.2	15.4
FZ Per	184	324	8.2	9.5	12.8
RW Cyg	550	676	12.9	14.2	17.2
SW Cep	70	234	9.8	6.7	9.8

FIGURE CAPTIONS

- Fig. 1. Evolutionary tracks of Population I stars with initial masses $M_{\text{ZAMS}} = 10, 15$ and $20M_{\odot}$ in the HR diagram. Parts of tracks corresponding to the stage of the red supergiant are shown in solid lines.
- Fig. 2. Variations of the gas flow velocity at the upper boundary U (a) and bolometric magnitude M_{bol} (b) in red supergiants with initial mass $M_{\text{ZAMS}} = 10M_{\odot}$ and luminosity $L = 2 \cdot 10^4$ (solid lines), $1.5 \cdot 10^4 L_{\odot}$ (dashed lines) and $10^4 L_{\odot}$ (dot-dashed lines).
- Fig. 3. The radial dependence of the mechanical work done by a Lagrangean mass zone over the pulsation period Π .
- Fig. 4. (a) – Variations of gas density ρ (solid line), temperature T (dashed line) and opacity κ (dotted line) in the layer of fully ionized helium; (b) – variations of radiative luminosity in units of the total equilibrium luminosity L_0 .
- Fig. 5. Same as Fig. 4 but for the layer with partial helium ionization.
- Fig. 6. The amplitude of variations of the total luminosity L_r expressed in units of the equilibrium luminosity L_0 versus the radial distance from the stellar center.
- Fig. 7. Kinetic energy of pulsation motions E_K (a) and the upper boundary radius R (b) as a function of time t for the hydrodynamical model $M_{\text{ZAMS}} = 16M_{\odot}$, $L = 8.5 \cdot 10^4 L_{\odot}$.
- Fig. 8. The period–luminosity diagram for red supergiants with initial masses $M_{\text{ZAMS}} = 10, 15$ and $20M_{\odot}$. Hydrodynamical models are represented by filled circles. In triangles are shown hydrodynamical models of stars that leave the red supergiant domain. In open circles are represented the hydrodynamical models of stars with central helium abundance $Y_c \leq 2.4 \cdot 10^{-3}$.
- Fig. 9. The period–mass diagram of red supergiants $8M_{\odot} \leq M_{\text{ZAMS}} \leq 20M_{\odot}$. Hydrodynamical models of stars with maximum and minimum equilibrium luminosity are shown by filled and open circles, respectively. Arrows indicate the direction of evolutionary change of the pulsation period Π of stars $M_{\text{ZAMS}} = 10M_{\odot}$ and $20M_{\odot}$. The region of allowed values of the radial pulsation periods is limited by dashed lines.
- Fig. 10. The pulsation constant Q of red supergiants $8M_{\odot} \leq M_{\text{ZAMS}} \leq 20M_{\odot}$ as a function of mass–to–radius ratio $f = (M/M_{\odot})/(R/R_{\odot})$. Hydrodynamical models of red supergiants are shown by filled circles.

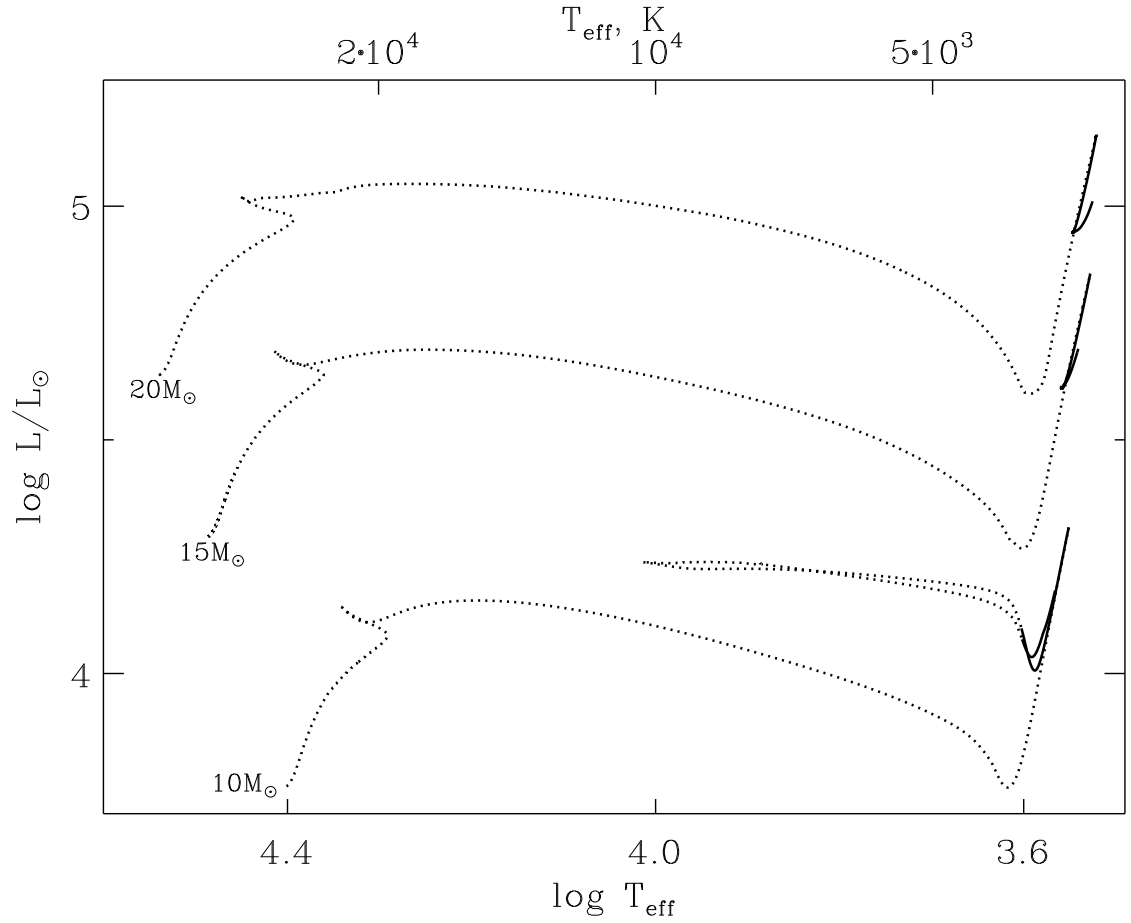


Figure 1: Evolutionary tracks of Population I stars with initial masses $M_{\text{ZAMS}} = 10, 15$ and $20M_{\odot}$ in the HR diagram. Parts of tracks corresponding to the stage of the red supergiant are shown in solid lines.

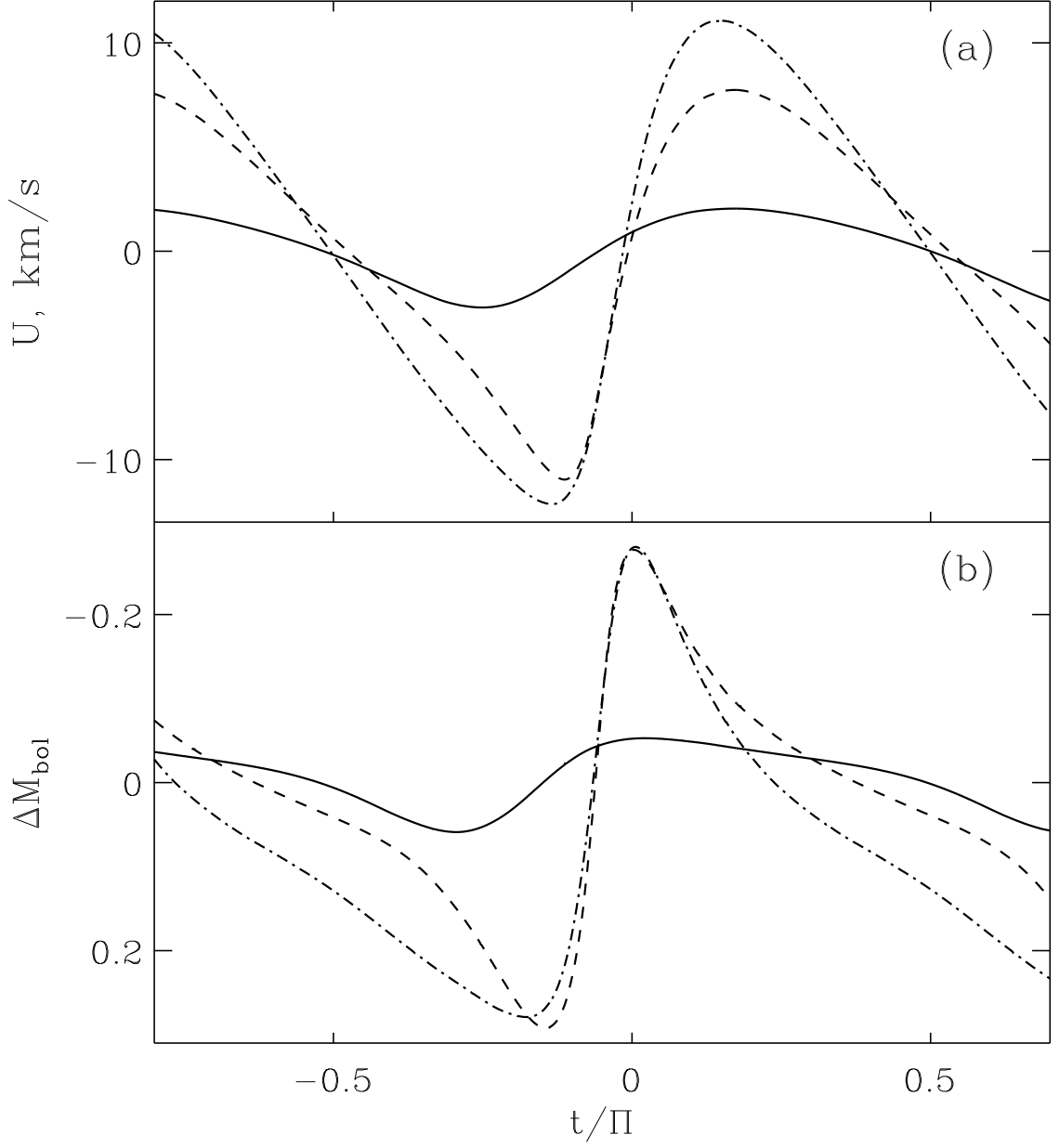


Figure 2: Variations of the gas flow velocity at the upper boundary U (a) and bolometric magnitude M_{bol} (b) in red supergiants with initial mass $M_{\text{ZAMS}} = 10M_\odot$ and luminosity $L = 2 \cdot 10^4$ (solid lines), $1.5 \cdot 10^4 L_\odot$ (dashed lines) and $10^4 L_\odot$ (dot-dashed lines).

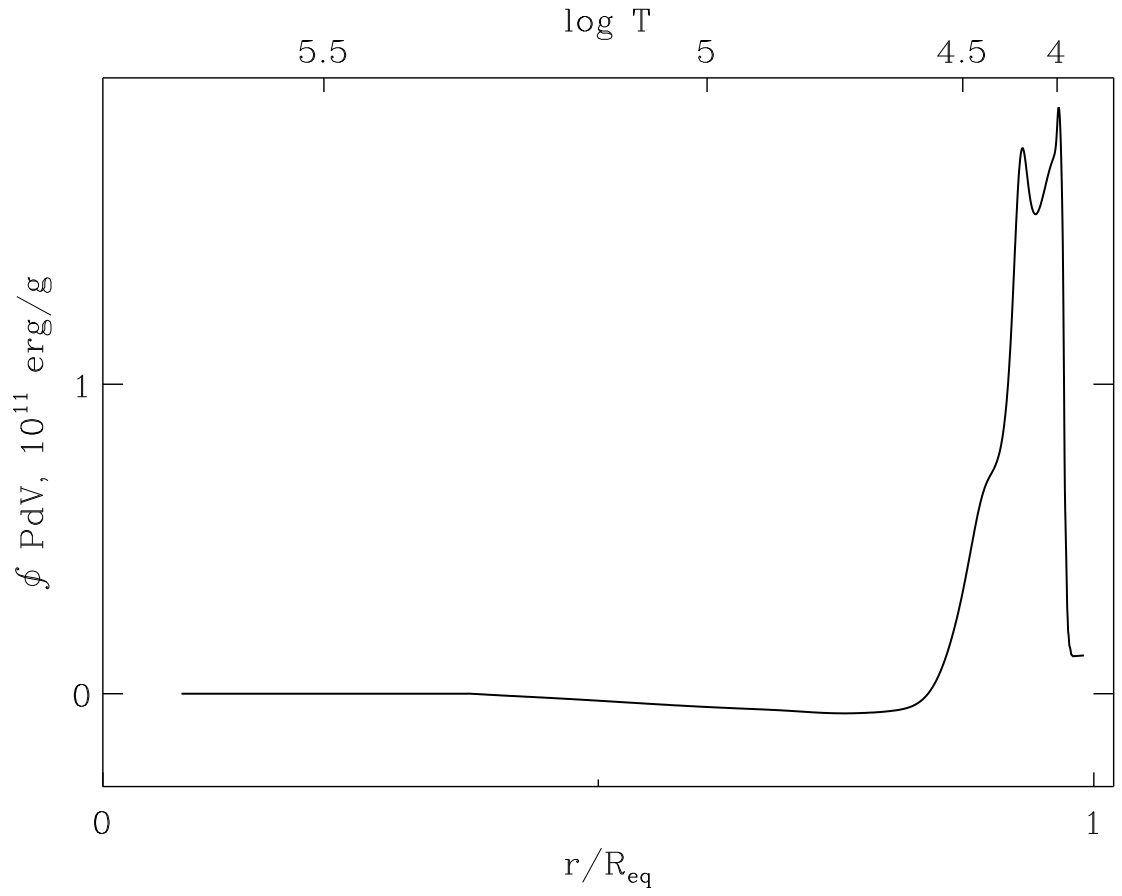


Figure 3: The radial dependence of the mechanical work done by a Lagrangean mass zone over the pulsation period II.

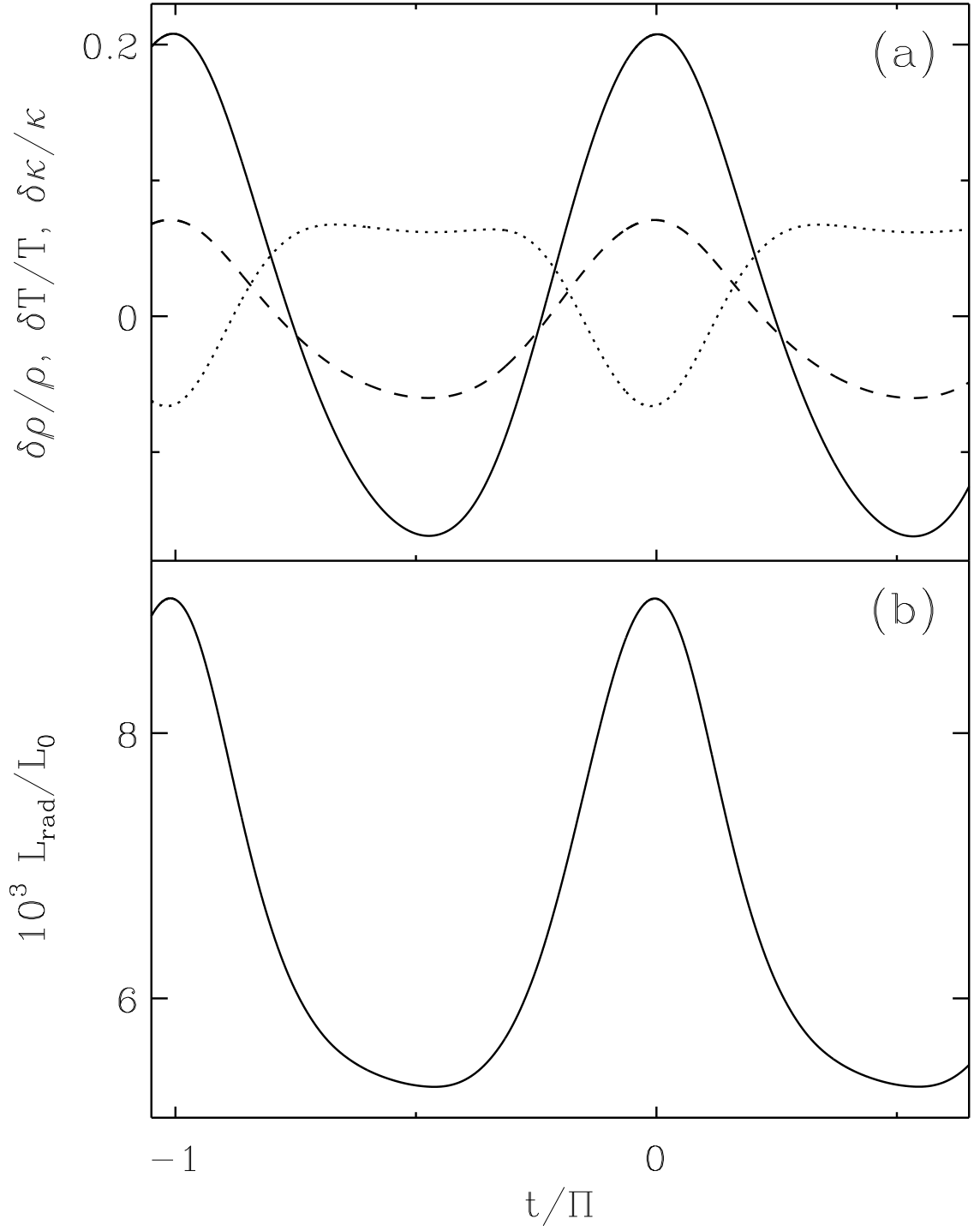


Figure 4: (a) – Variations of gas density ρ (solid line), temperature T (dashed line) and opacity κ (dotted line) in the layer of fully ionized helium; (b) – variations of radiative luminosity in units of the total equilibrium luminosity L_0 .

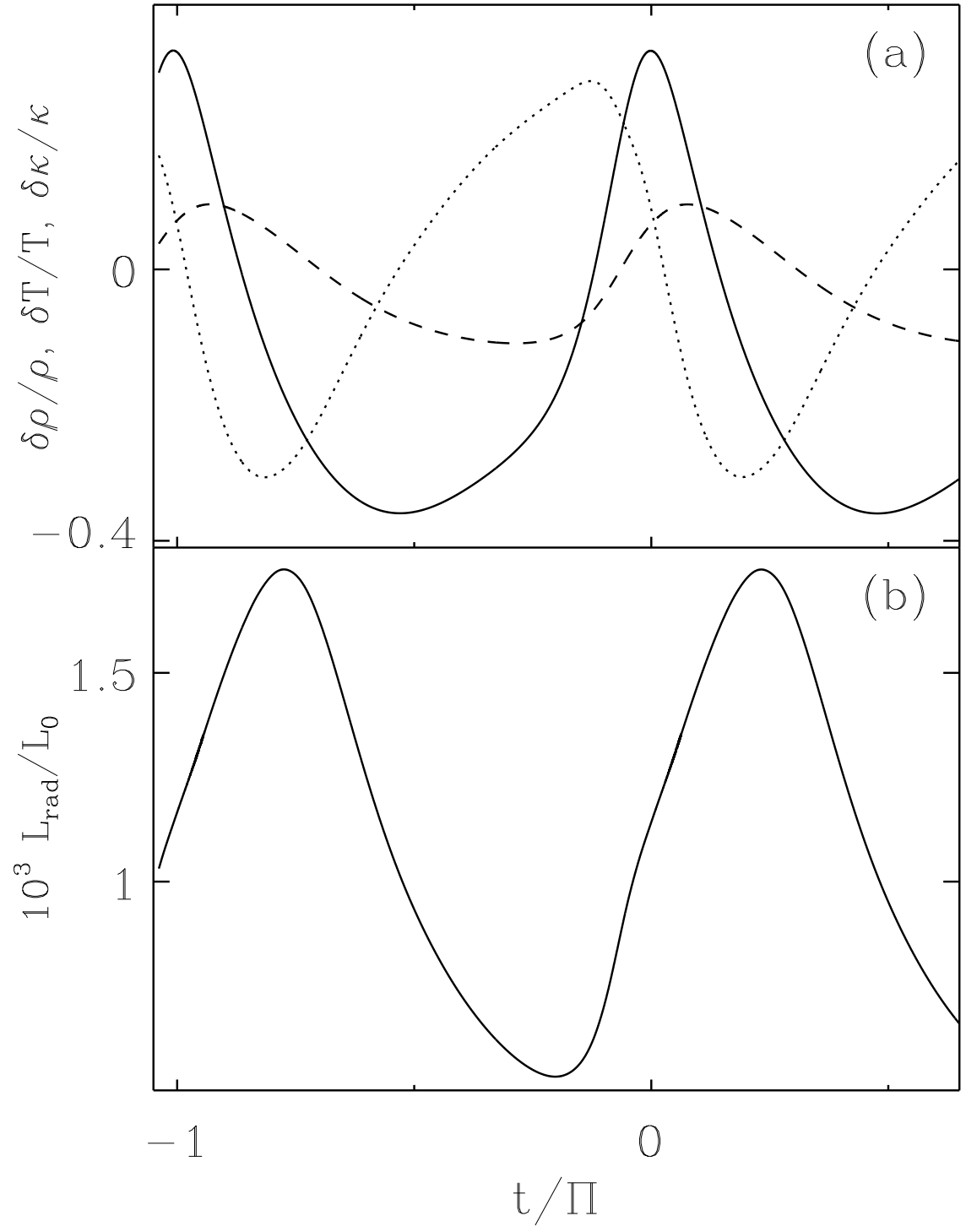


Figure 5: Same as Fig. 4 but for the layer with partial helium ionization.

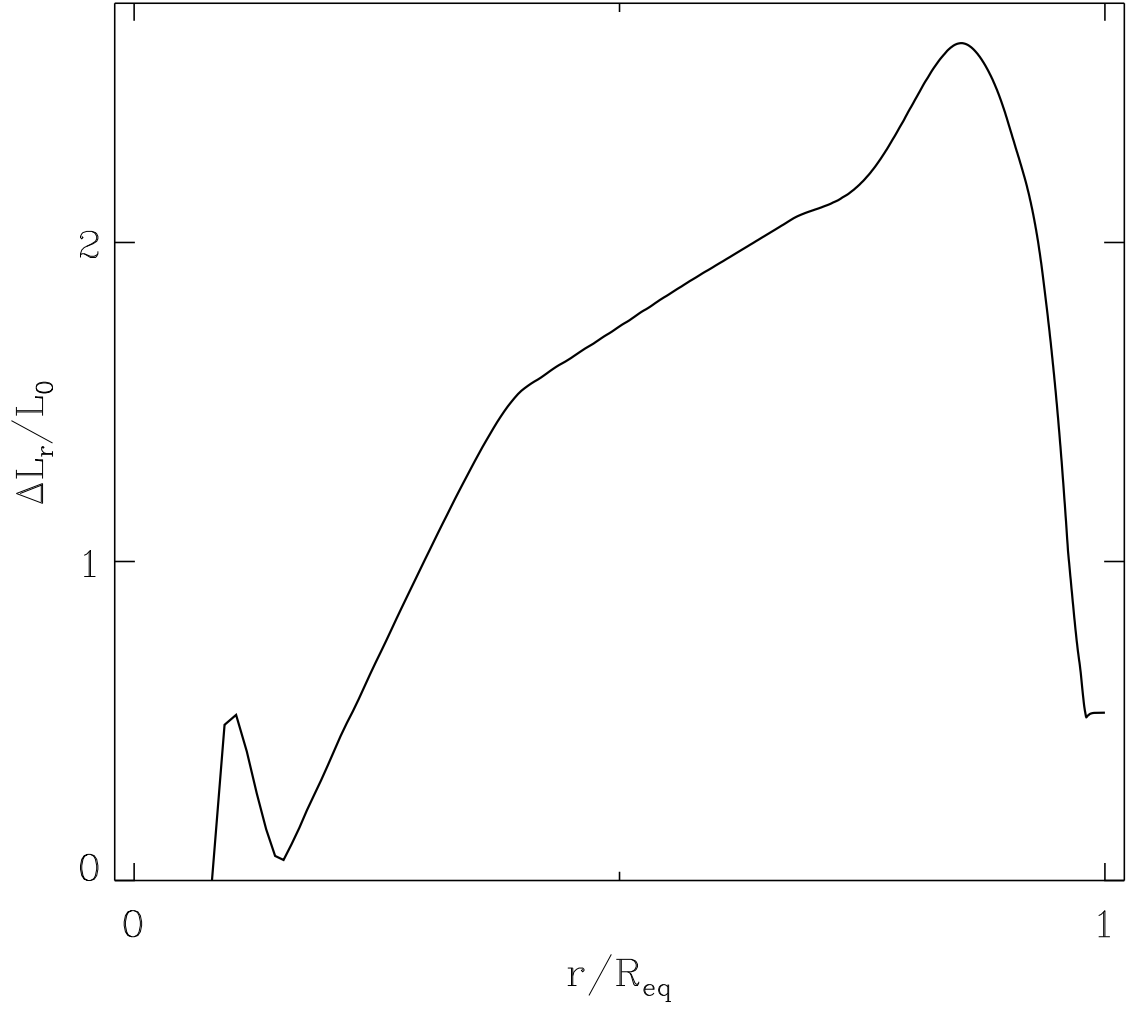


Figure 6: The amplitude of variations of the total luminosity L_r expressed in units of the equilibrium luminosity L_0 versus the radial distance from the stellar center.

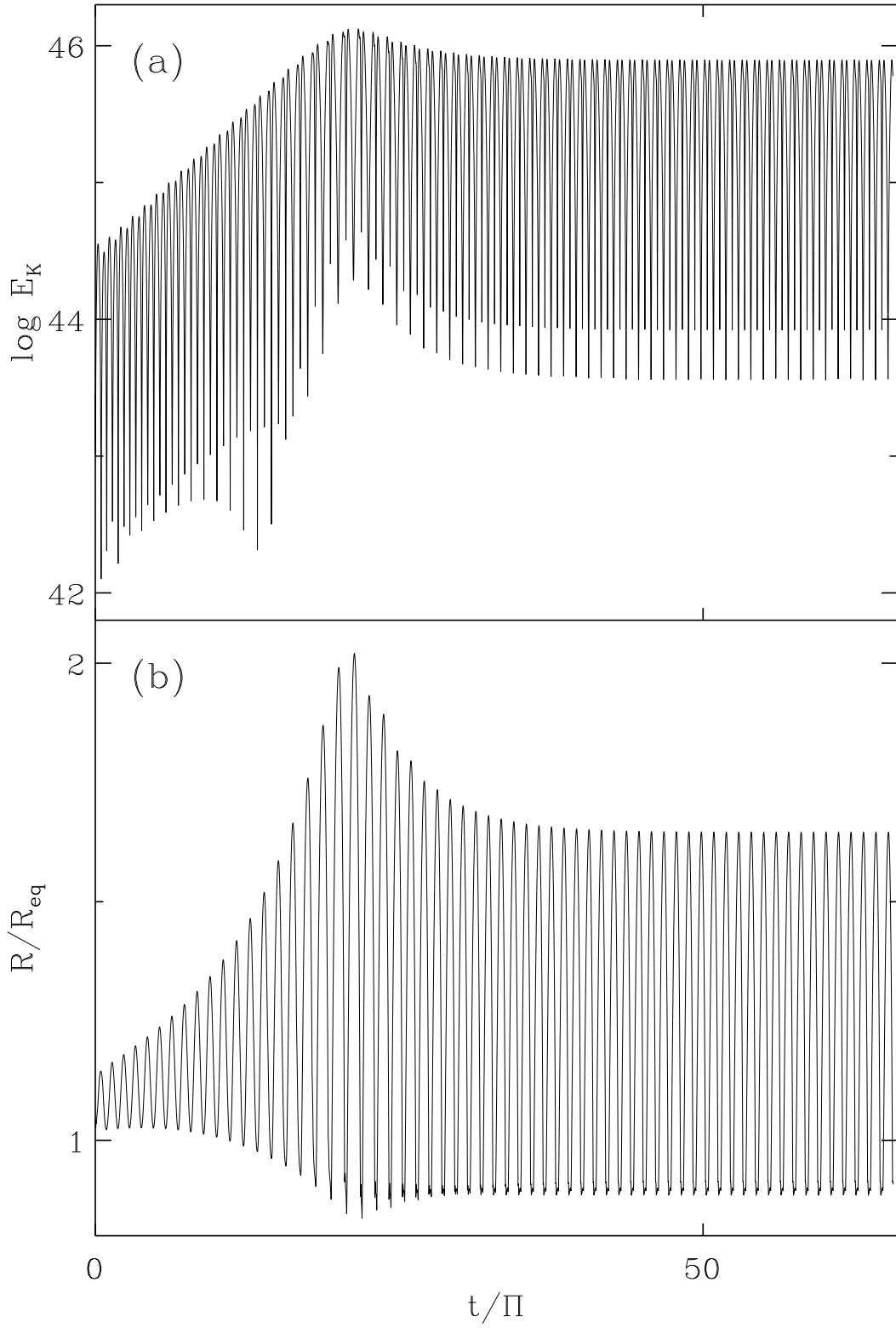


Figure 7: Kinetic energy of pulsation motions E_K (a) and the upper boundary radius R (b) as a function of time t for the hydrodynamical model $M_{\text{ZAMS}} = 16M_{\odot}$, $L = 8.5 \cdot 10^4 L_{\odot}$.

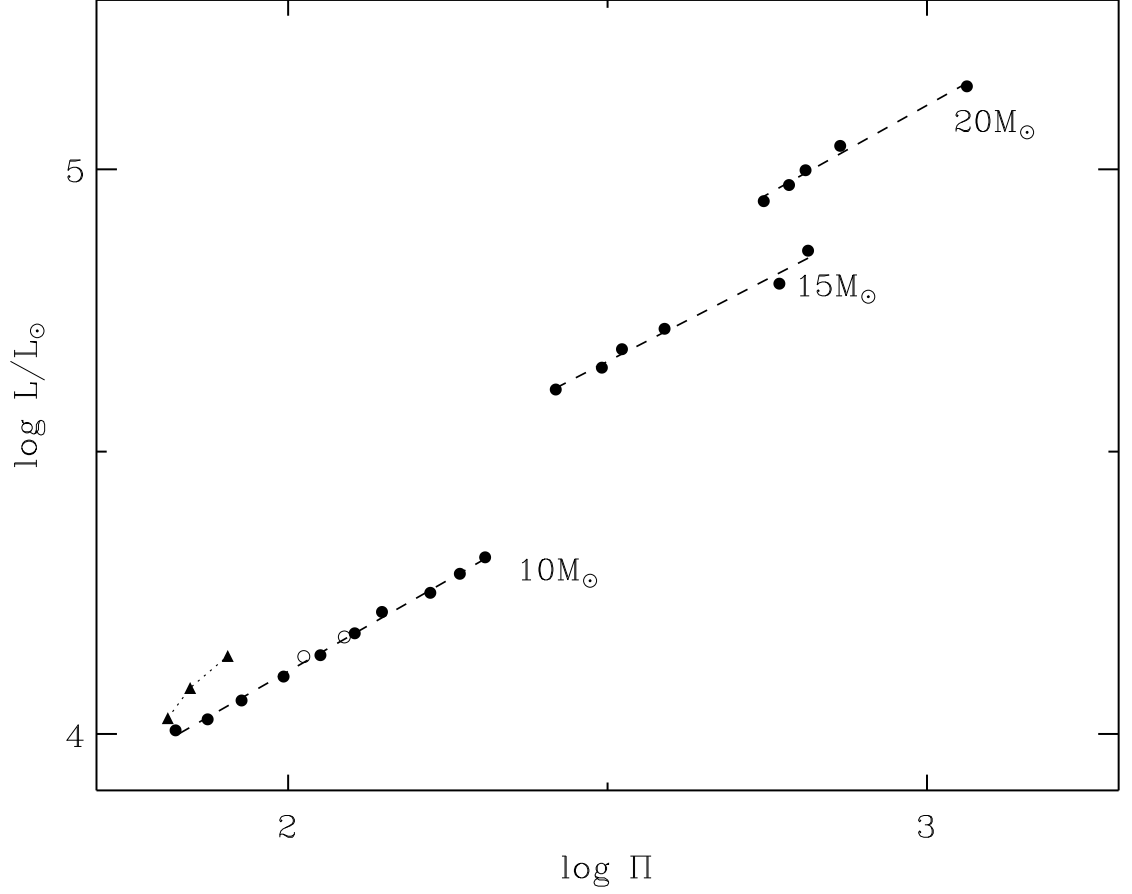


Figure 8: The period–luminosity diagram for red supergiants with initial masses $M_{\text{ZAMS}} = 10$, 15 and $20M_{\odot}$. Hydrodynamical models are represented by filled circles. In triangles are shown hydrodynamical models of stars that leave the red supergiant domain. In open circles are represented the hydrodynamical models of stars with central helium abundance $Y_c \leq 2.4 \cdot 10^{-3}$.

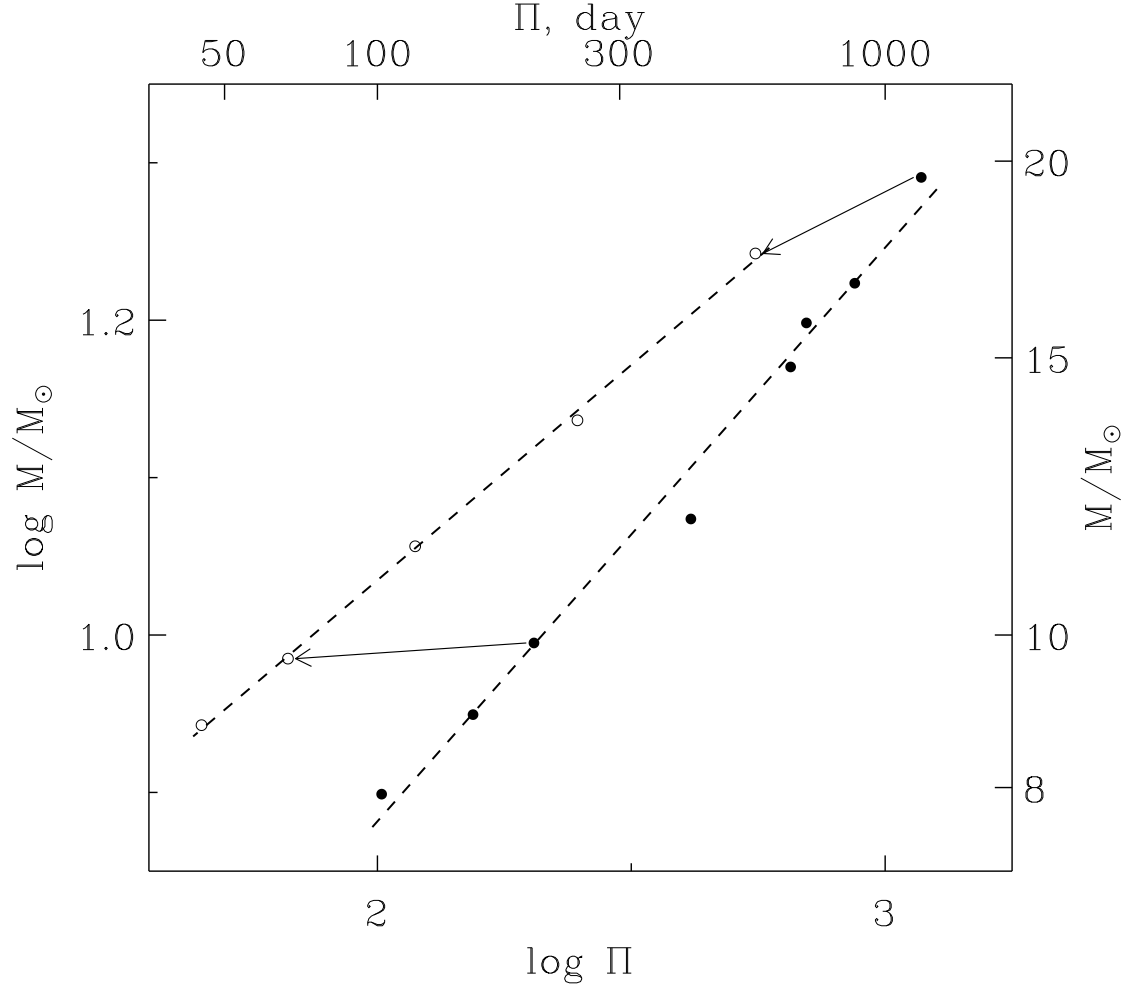


Figure 9: The period–mass diagram of red supergiants $8M_{\odot} \leq M_{\text{ZAMS}} \leq 20M_{\odot}$. Hydrodynamical models of stars with maximum and minimum equilibrium luminosity are shown by filled and open circles, respectively. Arrows indicate the direction of evolutionary change of the pulsation period Π of stars $M_{\text{ZAMS}} = 10M_{\odot}$ and $20M_{\odot}$. The region of allowed values of the radial pulsation periods is limited by dashed lines.

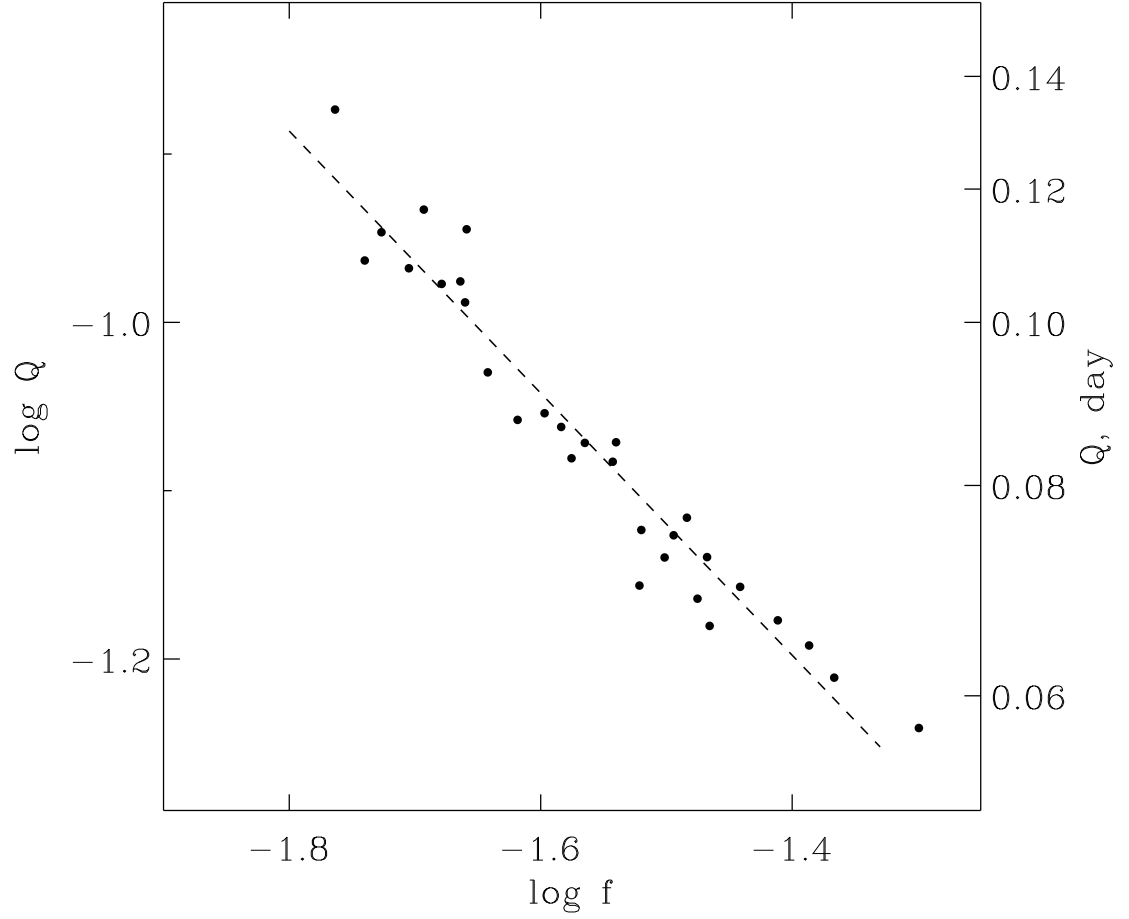


Figure 10: The pulsation constant Q of red supergiants $8M_{\odot} \leq M_{\text{ZAMS}} \leq 20M_{\odot}$ as a function of mass-to-radius ratio $f = (M/M_{\odot})/(R/R_{\odot})$. Hydrodynamical models of red supergiants are shown by filled circles.